Multiwavelength Properties of Infrared-faint Radio Sources Based on Analysis of Their Spectral Energy Distribution

(article starts on next page)

Multiwavelength Properties of Infrared-faint Radio Sources Based on Analysis of Their Spectral Energy Distribution

Yihang Zhang (张迤航)[1,2], Lulu Fan (范璐璐)[1,2,3], Tao An (安涛)[4], Jun Yang (杨军)[5], Weibin Sun (孙卫斌)[1,2], Haoran Yu (于浩然)[1,2], and Yunkun Han (韩云坤)[6,7,8,9]

[1] Department of Astronomy, University of Science and Technology of China, Hefei 230026, People's Republic of China; zhang_yh@mail.ustc.edu.cn, llfan@ustc.edu.cn

[2] School of Astronomy and Space Science, University of Science and Technology of China, Hefei 230026, People's Republic of China

[3] Deep Space Exploration Laboratory, Hefei 230088, People's Republic of China

[4] Key Laboratory of Radio Astronomy, Shanghai Astronomical Observatory, 80 Nandan Road, 200030 Shanghai, People's Republic of China

[5] Department of Space, Earth and Environment, Chalmers University of Technology, Onsala Space Observatory, SE-439 92 Onsala, Sweden

[6] Yunnan Observatories, Chinese Academy of Sciences, 396 Yangfangwang, Guandu District, Kunming 650216, People's Republic of China

[7] Center for Astronomical Mega-Science, Chinese Academy of Sciences, 20A Datun Road, Chaoyang District, Beijing 100012, People's Republic of China

[8] Key Laboratory for the Structure and Evolution of Celestial Objects, Chinese Academy of Sciences, 396 Yangfangwang, Guandu District, Kunming 650216, People's Republic of China

[9] International Centre of Supernovae, Yunnan Key Laboratory, Kunming 650216, People's Republic of China

Abstract

Infrared-faint radio sources (IFRSs) are believed to be a rare class of radio-loud active galactic nuclei (AGNs) characterized by their high radio-to-infrared flux density ratios of up to several thousand. Previous studies have shown that a fraction of IFRSs are likely to be hosted in dust-obscured galaxies. In this paper, our aim is to probe the dust properties, star formation rate (SFR), and AGN activity of IFRSs by modeling the UV-to-infrared spectral energy distribution (SED) of 20 IFRSs with spectroscopic redshifts ranging from 1.2 to 3.7. We compare the Bayesian evidence of a three-component model (stellar, AGN, and cold dust) with that of a two-component model (stellar and cold dust) for six IFRSs in our sample with far-infrared photometry and find that the three-component model has significantly higher Bayesian evidence, suggesting that IFRSs are most likely to be AGNs. The median SED of our IFRS sample shows similarities to an AGN–starburst composite in the IR regime. The derived IR luminosities of IFRSs indicate that they are low-luminosity counterparts of high-redshift radio galaxies. We disentangle the contributions of AGN-heated and star formation-heated dust to the IR luminosity of IFRSs and find that our sample is likely AGN-dominated. However, despite the evidence for significant impact of an AGN on the host galaxy, the AGN luminosity of our sample does not show correlation with the SFR of the sources.

Unified Astronomy Thesaurus concepts: Active galaxies (17); Radio galaxies (1343); Active galactic nuclei (16)

1. Introduction

Infrared-faint radio sources (IFRSs) are rare galaxies that are bright at radio wavelengths but extremely faint in the near-infrared (NIR) regime. They were first discovered by R. P. Norris et al. (2006) as radio sources detected at $\lambda = 20$ cm in the deep radio observations of the Australia Telescope Large Area Survey (ATLAS) in Chandra Deep Field South (CDFS) but without counterparts in the Spitzer Wide-area Infrared Extragalactic Survey (SWIRE) at $\lambda = 3.6$, 4.5, 5.8, 8.0, and 24 μm. This discovery was quite surprising, since it is generally assumed that active galactic nuclei (AGNs) and star-forming galaxies (SFGs) detectable at $\lambda = 20$ cm would also be detectable by SWIRE. 31 more sources were found in the European Large Area IR Space Observatory Survey South 1 (ELAIS-S1) field (E. Middelberg et al. 2008a). The IFRSs found in these deep fields have a 1.4 GHz flux density range from a few hundred μJy to a few tens of mJy, while nondetection in the SWIRE imposes an upper flux limit of 5 μJy in the 3.6 μm band. In particular, all 53 IFRS found in CDFS and ELAIS-S1 lack optical counterparts.

Early research characterized IFRSs as sources without a detectable counterpart at any Spitzer wavelength, which is a rather loose definition and depends on the sensitivity of the survey (R. P. Norris et al. 2006). P. C. Zinn et al. (2011) proposed a new set of IFRS selection criteria independent of surveys. A source is identified as an IFRS if the two following conditions are met: (i) flux density ratio $S_{20cm}/S_{3.6\mu m} > 500$; (ii) $S_{3.6\mu m} < 30$ μJy. The first criterion selects sources with extreme radio-to-IR flux density ratios, excluding contamination from SFGs. The second criterion ensures that low-redshift AGNs are not selected, as they typically exhibit a relatively high flux density in the IR. P. C. Zinn et al. (2011)'s criteria enable the search of a larger, brighter IFRS population with optical and infrared detections. Using these criteria, J. D. Collier et al. (2014) searched for IFRSs using data from the Unified Radio Catalog (URC; A. E. Kimball & Ž. Ivezić 2008) and the Wide-field Infrared Survey Explorer (WISE; E. L. Wright et al. 2010) and compiled a sample of 1317 IFRSs, which is the largest IFRS sample by far.

Previous investigations of IFRSs that focused on radio wavelengths suggested that they are young radio-loud active galactic nuclei (RL AGNs). Very long baseline interferometry (VLBI) observations of some IFRSs showed brightness temperatures of about 10^6 K, indicating nonthermal emission from AGNs (R. P. Norris et al. 2007; E. Middelberg et al. 2008b; A. Herzog et al. 2015a). Most VLBI-detected IFRSs show compact cores, suggesting that they contain young AGNs whose jets have not expanded yet (A. Herzog et al. 2015a). A
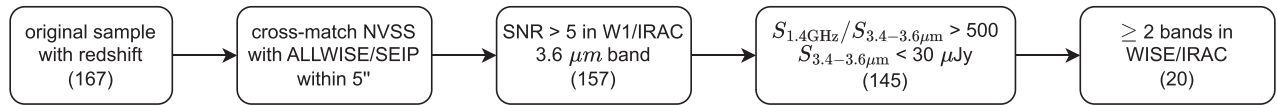
Figure 1. Flowchart of our sample selection process. The numbers in parentheses indicate the number of sources remaining after each step of selection.

substantial fraction of IFRSs are compact steep-spectrum (CSS) and GHz-peaked-spectrum (GPS) sources (E. Middelberg et al. 2011; J. D. Collier et al. 2014; A. Herzog et al. 2016). GPS sources exhibit a turnover in the spectrum at ∼1 GHz and are considered to represent the earliest evolutionary stage of AGNs (K. E. Randall et al. 2011). CSS sources are compact radio sources with a spectral peak at ∼100 MHz and a steep spectral index across the GHz range ($\alpha \leqslant -0.8$). CSS sources are more extended than GPS sources and possibly represent an intermediate evolutionary phase between GPS sources and the larger Fanaroff–Riley type I/II (FR I/ FR II) galaxies. The IFRSs identified in the ELAIS-S1 field have steep radio spectra with a median index of $\alpha = -1.4$ between 2.3 and 8.4 GHz (E. Middelberg et al. 2011), which is steeper than the general radio source population ($\alpha = -0.86$) and the AGN source population ($\alpha = -0.82$) in ELAIS-S1, further supporting that a substantial fraction of IFRSs contain young AGNs.

Using ultradeep Spitzer imaging, IR counterparts of some IFRSs were detected, while upper flux limits in the IRAC bands for nondetected sources were attained through image stacking. IR-to-radio spectral energy distribution (SED) modeling of IFRSs showed that 3C sources can reproduce the data when redshifted to $z > 2$ (T. Garn & P. Alexander 2008; M. T. Huynh et al. 2010). A. Herzog et al. (2015b) stacked Herschel maps to obtain upper limits on the far-infrared (FIR) flux density of six IFRSs. Combined with radio detections and upper limits on SWIRE flux density, their SED modeling found that known RL quasar templates failed to match the photometric constraints of IFRSs, but RL quasar or CSS sources at lower redshifts ($z \leqslant 5$) with additional dust obscuration could reproduce the IR-faintness of IFRSs. Spectroscopic redshifts of IFRSs are crucial for accurate SED modeling and decomposition. Due to their faintness in the optical and IR regimes, it has been difficult to measure the spectroscopic redshifts of IFRSs. The first such redshifts were presented by J. D. Collier et al. (2014) and A. Herzog et al. (2014), who identified the redshifts of 21 IFRSs within the range $1.8 \leqslant z \leqslant 3.0$. These sources with measured spectroscopic redshifts lie at the IR-bright end of IFRSs, with IR flux densities between 14 μJy and 30 μJy at 3.6 μm or 3.4 μm, implying that the IR-fainter ones are located at even higher redshifts. B. J. Orenstein et al. (2019) presented the largest sample of IFRSs with spectroscopic redshifts, containing 131 sources with a median redshift of $z = 2.68$.

The flux density ratio $S_{1.4\,\text{GHz}}/S_{3.6\mu\text{m}}$ of IFRSs substantially overlaps with that of high-redshift radio galaxies (HzRGs), ranging from several hundred to several thousand, which is uncommon for general radio sources (N. Seymour et al. 2007; R. P. Norris et al. 2011). HzRGs are a class of powerful radio galaxies ($L_{3\,\text{GHz}} > 10^{26}\,\text{W Hz}^{-1}$) at high redshifts ($1 \leqslant z \leqslant 5$). They are believed to be the progenitors of the most massive galaxies in the local Universe (N. Seymour et al. 2007; C. De Breuck et al. 2010). A potential link between IFRSs and HzRGs has been suggested, as HzRGs are the only high-redshift population known to exhibit the same extreme radio-to-IR flux density ratios. A. Herzog et al. (2015b) found that the SEDs of

their IFRS sample could be explained by HzRG templates at even higher redshifts ($z > 5$) or with additional dust extinction. Besides these similarities, a notable difference between IFRSs and HzRGs is that HzRGs are known to host highly accreting AGNs and vigorous star formation, both of which contribute to their high mid- and far-IR luminosities. IFRSs could be fainter, higher-redshift siblings of HzRGs. SED modeling of IFRSs constrained by spectroscopic redshift and optical-to-IR photometric data could uncover the nature of IFRSs and test the possible relation between IFRSs and HzRGs.

In this paper, we present a redshift-based optical-to-IR SED modeling of 20 IFRSs. Using a Bayesian approach, we decompose the emissions from different components and find strong evidence for AGNs in IFRSs. In Section 2, we describe our sample selection and the construction of an optical-to-IR SED. In Section 3, we introduce our Bayesian method for SED modeling. We present our results of SED modeling in Section 4. In Section 5, we discuss the parameters derived from the SED modeling and the possible nature of IFRSs. We summarize our conclusions in Section 6.

2. Sample Selection and Multiwavelength Data

2.1. Sample Selection

J. D. Collier et al. (2014) slightly modified P. C. Zinn et al. (2011)'s criteria by replacing the 3.6 μm flux density with the 3.4 μm flux density from WISE (E. L. Wright et al. 2010), which enables the construction of a significantly larger IFRS sample.

To build a sample for SED modeling, we started with the 167 IFRSs that had been identified with spectroscopic redshifts (J. D. Collier et al. 2014; A. Herzog et al. 2016; V. Singh et al. 2017; B. J. Orenstein et al. 2019). We obtained the 20 cm radio data for 167 IFRSs from the URC version 2.0 compiled by A. E. Kimball & Ž. Ivezić (2014). This radio catalog contains data from the NRAO VLA Sky Survey (NVSS; J. J. Condon et al. 1998), Faint Images of the Radio Sky at Twenty Centimeters (FIRST; R. H. Becker et al. 1995), Green Bank 6 cm survey (GB6; P. C. Gregory et al. 1996), the Westerbork Northern Sky Survey (R. B. Rengelink et al. 1997), and the Sloan Digital Sky Survey Data Release 9 (SDSS DR9; C. P. Ahn et al. 2012). The 3.4 and 3.6 μm data are from the ALLWISE data release (R. M. Cutri et al. 2021) and Spitzer Enhanced Imaging Products (SEIP; P. Capak 2019), respectively. We applied the following criteria to select the sample discussed in this paper:

(i) We cross-matched the NVSS positions to ALLWISE and SEIP with a search radius of 5″ and applied a signal-to-noise ratio limit of S/N ⩾ 5 in the W1 band and the IRAC band 1.

(ii) We selected all sources with $S_{20\text{cm}}/S_{3.4-3.6\mu\text{m}} \geqslant 500$.

(iii) We selected all sources with $S_{3.6\mu\text{m}} \leqslant 30\,\mu\text{Jy}$.

The complete selection process of our sample is shown in Figure 1. After applying the selection criteria mentioned above,

our final sample consisted of 145 IFRSs with spectroscopic redshifts. To construct the UV-to-IR SEDs for IFRSs, we retrieved multiwavelength photometry from various catalogs, which will be discussed in the next section.

2.2. Infrared Data

The W1, W2, and W3 photometry for the IFRS sample is from the ALLWISE data release (R. M. Cutri et al. 2021). To convert the catalog Vega magnitudes to flux density in janskys (Jy), we used flat color correction factors determined for IFRSs by J. D. Collier et al. (2014), which are

$$S_{W1} = 306.682 \times 10^{-M_{W1}/2.5} \text{ Jy} \tag{1}$$

$$S_{W2} = 170.663 \times 10^{-M_{W2}/2.5} \text{ Jy} \tag{2}$$

$$S_{W3} = 29.045 \times 10^{-M_{W3}/2.5} \text{Jy.} \tag{3}$$

32 IFRSs in our sample have NIR broadband photometric data from different surveys, including the eighth data release of the United Kingdom Infrared Telescope (UKIRT) Infrared Deep Sky Survey (UKIDSS DR8; A. Lawrence et al. 2012) in the J, H, and K bands and the Visible and Infrared Survey Telescope for Astronomy (VISTA) Deep Extragalactic Observations Survey (VIDEO; M. Jarvis 2012) in the Z, Y, J, H, and K_s bands. 15 IFRSs in our sample have mid-infrared (MIR) data from the SEIP (P. Capak 2019) Source List, which includes data from the four bands of the Infrared Array Camera (IRAC; G. G. Fazio et al. 2004) and the 24 μm band of the Multiband Imaging Photometer (MIPS; G. H. Rieke et al. 2004). For FIR photometry, six IFRSs in our sample have Herschel Photoconductor Array Camera and Spectrometer (PACS; A. Poglitsch et al. 2010) observations at 70 and 160 μm and Spectral and Photometric Imaging Receiver (SPIRE; M. J. Griffin et al. 2010) observations at 250, 350, and 500 μm. The IR photometry of the six sources is listed in Table 1

2.3. Optical Data

129 IFRSs in our sample have optical counterparts in SDSS Data Release 17 (Abdurro'uf et al. 2022), the Canada–France–Hawaii Telescope Legacy Survey (CFHTLS; P. Hudelot et al. 2012), and the Multi-wavelength Survey by Yale–Chile optical imaging in ECDF-S (MUSYC; C. N. Cardamone et al. 2010).

In order to obtain reliable estimations on the properties of IFRSs, we selected 20 IFRSs with counterparts in at least two bands in ALLWISE or the SEIP Source List from the original sample for SED modeling. Their redshift, 20 cm, and 3.4/3.6 μm data are listed in Table 2. Figure 2 provides a more intuitive illustration of the redshift and flux density ratio $S_{20cm}/S_{3.4-3.6\mu m}$ distributions for the original and selected samples. To assess the representativeness of our selected sample of 20 IFRSs, we conducted a Kolmogorov–Smirnov (K-S) test on both the redshift distributions and the radio-to-IR flux density ratios. These two K-S tests resulted in p-values of 0.066 and 0.105, respectively, which are marginally above the commonly used significance threshold of 0.05. This suggests a potential, though not statistically significant, difference in the distributions of redshift and radio-to-IR flux density ratio between the selected and original samples. The K-S tests imply that there may be a slight bias in our selection, which will be

considered when interpreting the results of the SED analysis for the selected IFRS sample.

3. SED Modeling

For the SED analysis of our IFRS sample, we used the latest version of the Bayesian SED modeling and interpretation code BayeSED V3.0 (Y. Han & Z. Han 2014, 2019; Y. Han et al. 2023).[10] This updated version has been tested on mock galaxy samples and has demonstrated accuracy and speed in estimating galaxy parameters. BayeSED employs principal component analysis to reduce the dimensionality of the model SED library. Then, it utilizes an artificial neural network or K-nearest neighbors searching to generate and evaluate the model SED at any point in the parameter space. The MultiNest sampling algorithm is used to obtain the posterior probability distribution of the parameters and Bayesian evidence of the SED model used.

To understand the physical mechanism responsible for their extreme radio-to-IR flux density ratios, we need to determine the relative contributions of different components. The stellar emission is modeled by using the G. Bruzual & S. Charlot (2003) simple stellar population (SSP) library with the G. Chabrier (2003) initial mass function, an exponentially declining star formation history (SFH), and the D. Calzetti et al. (2000) dust attenuation law. The free parameters in stellar component modeling include stellar age, timescale τ of the declining SFH, stellar metallicity Z, and dust attenuation A_V. The IR emission could come from hotter AGN-heated dust and/or colder star formation-heated dust. We assumed an energy balance between stellar emission and cold dust emission, where the stellar emission absorbed by cold dust was completely reemitted in the IR regime. The cold dust emission was modeled by a graybody (GB), which was defined as

$$S_\lambda \propto (1 - e^{-(\lambda_0/\lambda)^\beta})B_\lambda(\lambda, T_{dust}) \tag{4}$$

where $\lambda_0 = 125 \mu$m and B_λ is the Planck blackbody spectrum. The free parameters of the GB model are the dust temperature T_{dust} and the emissivity index β. The AGN component is independently modeled using the CLUMPY torus model (M. Nenkova et al. 2008a, 2008b),[11] which is given as an extensively sampled library of AGN SEDs. The CLUMPY torus model has six free parameters: the ratio of the outer to inner radii $Y = R_0/R_d$, the observer's line-of-sight inclination i, the radial density profile index q ($\rho \propto r^{-q}$), the clump's optical depth τ_V, the number of clouds along a radial equatorial path N_0, and the width parameter σ of the angular distribution. The CLUMPY model includes not only the torus dust emission but also part of the AGN accretion disk emission, thus providing a consistent modeling of the UV-to-millimeter SED of AGNs. We assumed that the priors of the 12 free parameters followed truncated uniform distributions. The prior ranges are summarized in Table 3.

4. Results

4.1. Model Comparison

Of the 20 sources on which we conducted the SED fitting, six were detected in Herschel/SPIRE bands, where cold dust emission dominates. To determine the presence of an AGN

---

[10] https://github.com/hanyk/BayeSED3
[11] https://www.clumpy.org/

<div align="center">

Table 1
IR Photometry of Six IFRSs

</div>

| Source ID	3.6 μm[a] (μJy)	4.5 μm[a] (μJy)	5.8 μm[a] (μJy)	8 μm[a] (μJy)	24 μm[a] (mJy)	100 μm[b] (mJy)	160 μm[b] (mJy)	250 μm[b] (mJy)	350 μm[b] (mJy)	500 μm[b] (mJy)
122	42.33 ± 0.37	61.88 ± 0.58	92.28 ± 2.01	166.8 ± 3.56	0.57 ± 0.04	...	...	33.2 ± 7.60	44.0 ± 9.3	30.1 ± 8.6
136	11.04 ± 0.21	16.15 ± 0.71	35.85 ± 8.08	181.40 ± 10.55	13.4 ± 7.7	13.4 ± 7.71	38.98 ± 10.72	5.6 ± 2.3	12.1 ± 2.5	9.0 ± 3.4
154	4.76 ± 0.08	4.928 ± 0.09	5.485 ± 0.32	2.89 ± 0.3	0.18 ± 0.01	...	...	11.7 ± 3.8	13.2 ± 3.8	10.6 ± 4.0
160	27.34 ± 0.11	50.46 ± 0.19	110.3 ± 0.64	243.9 ± 1.23	0.87 ± 0.01	...	...	16.1 ± 2.4	14.6 ± 2.2	6.7 ± 2.6
161	11.4 ± 0.55	11.96 ± 0.88	48.59 ± 5.04	...	0.59 ± 0.05	...	...	3.8 ± 2.4	7.5 ± 4.5	...
162	13.4 ± 0.99	13.47 ± 0.14	18.56 ± 0.52	21.86 ± 0.9	0.35 ± 0.01	...	...	14.8 ± 1.1	15.1 ± 1.0	10.9 ± 1.4

Notes.
[a] 3.6, 4.5, 5.8, 8.0, and 24 μm photometry from Spitzer SEIP catalog (P. Capak 2019).
[b] 100, 160, 250, 350, and 500 μm photometry from Herschel Multi-tiered Extragalactic Survey (S. J. Oliver et al. 2012).
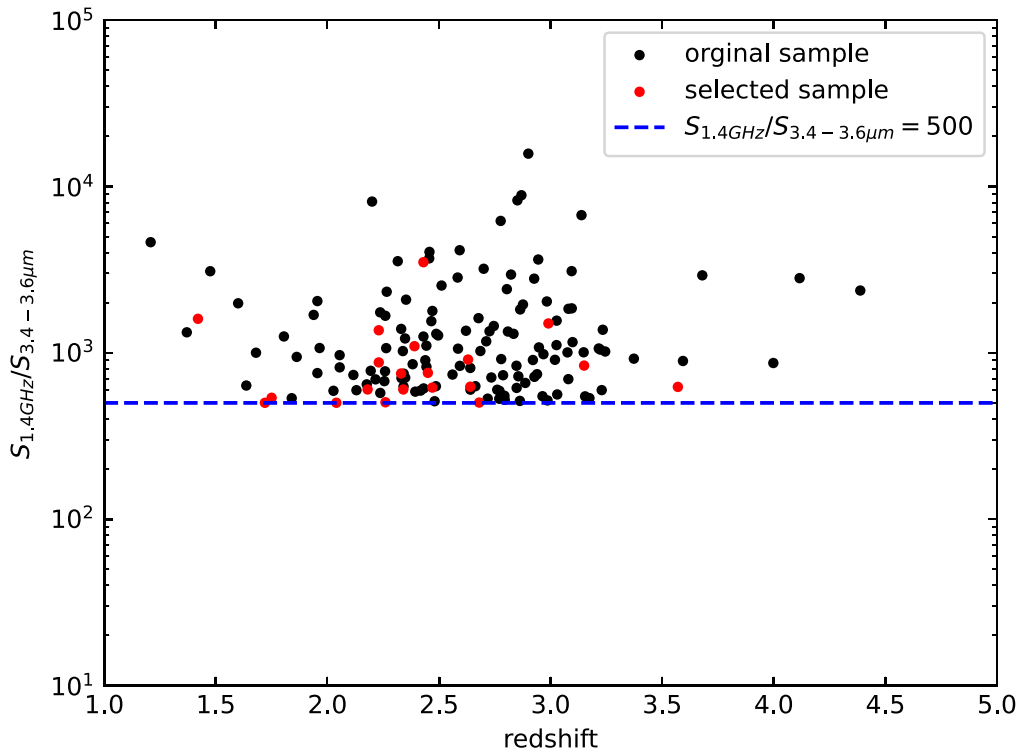
Figure 2. The distribution of radio-to-IR ratio vs. redshift of the original sample and the selected sample. The black dots represent the original IFRS sample. The red dots represent our selected sample of 20 IFRSs for SED modeling. The blue dashed line indicates the selection criterion for IFRS.

Table 2
The Sample of 20 IFRSs with Spectroscopic Redshift

Source ID	R.A. (J2000)	Decl. (J2000)	Redshift[a]	S_{20cm}[b] (mJy)	$S_{3.4/3.6\mu m}$[c] (μJy)
6	152.63407	8.13474	2.33	20.49	27.28
37	205.87463	32.13341	3.15	19.54	23.31
41	241.50610	29.53084	2.18	16.88	28.02
61	245.94765	54.71742	2.23	22.76	25.98
74	178.61794	14.16786	2.68	14.70	29.26
83	191.42380	25.98835	2.26	15.02	29.78
106	249.94554	40.65931	2.63	19.75	21.67
110	143.87793	61.28998	1.42	45.30	28.28
116	202.34253	5.33735	2.99	44.90	29.89
119	208.90853	6.18864	2.39	31.10	28.36
122	219.59085	34.66693	2.34	12.26	20.36
133	249.57249	41.45825	2.23	36.81	26.93
136	34.51425	−5.64040	3.57	8.91	14.28
154	53.31985	−28.00457	2.64	4.63	7.40
160	34.72328	−4.79341	2.47	16.90	27.34
161	36.53788	−4.55964	2.45	8.64	11.40
162	34.66483	−4.69710	2.43	50.82	14.49
164	34.62547	−5.28825	2.04	0.19	2.11
165	34.71386	−5.15043	1.75	16.01	29.82
166	34.50497	−4.70029	1.72	0.109	1.79

Notes.
[a] The spectroscopic redshifts are from A. Herzog et al. (2016), V. Singh et al. (2017), B. J. Orenstein et al. (2019), SDSS DR17 (Abdurro'uf et al. 2022), and the Dark Energy Spectroscopic Instrument (DESI) survey (DESI Collaboration et al. 2024).
[b] Flux density at 20 cm from FIRST catalog.
[c] Flux density at 3.4 μm and 3.6 μm from AllWISE and Spitzer SEIP catalogs.

component in IFRSs, we performed two-component (SSP +GB) and three-component (SSP+Torus+GB) SED modeling on the six IFRSs. Figure 3 shows the best-fitting results of

IFRS 161 with and without the AGN torus model. In the case of IFRS 161, the SSP+Torus+GB model seems to provide a better fit to the observations than the SSP+GB model. However, the SSP+Torus+GB model also introduces more free parameters than the SSP+GB model. According to the principle of Occam's razor, a simpler model with a compact parameter space should be preferred over a more complicated one, unless the latter can provide a significantly better explanation of the data (Y. Han & Z. Han 2019). To compare different models quantitatively, we chose to use Bayesian evidence rather than the Bayesian information criterion (BIC) because Bayesian evidence provides a more comprehensive framework. Bayesian evidence integrates over the entire parameter space and accounts for uncertainty in parameter estimates and prior distributions, whereas BIC only offers asymptotic approximations to Bayesian evidence. Furthermore, Bayesian evidence is better suited for comparing complex models, such as our multicomponent SED models, especially with a relatively small sample size. The SSP+Torus+GB model will have lower Bayesian evidence unless it provides a significantly better fit than the SSP+GB model.

In Table 4, we present the natural logarithms $\ln(ev_{AGN})$ and $\ln(ev_{no\ AGN})$ of Bayesian evidence and the Bayes factor $\ln(ev_{AGN}/ev_{noAGN})$ for the two models. We find that the SSP +Torus+GB model has significantly higher Bayesian evidence than the SSP+Torus model for all IFRSs in the subsample. According to the empirically calibrated Jeffrey scale (C. P. Robert et al. 2008; R. Trotta 2008), $\ln(ev_{AGN}/ev_{noAGN}) > 5$ (corresponding to odds of about 150:1) indicates strong evidence in favor of an AGN torus component in IFRSs. Therefore, we utilize the results of the three-component model in the following discussion. In Figure 4, we show the best-fit SEDs of six IFRSs with the three-component models. Absorbed stellar emission, AGN emission, and cold dust emission are represented by the blue,
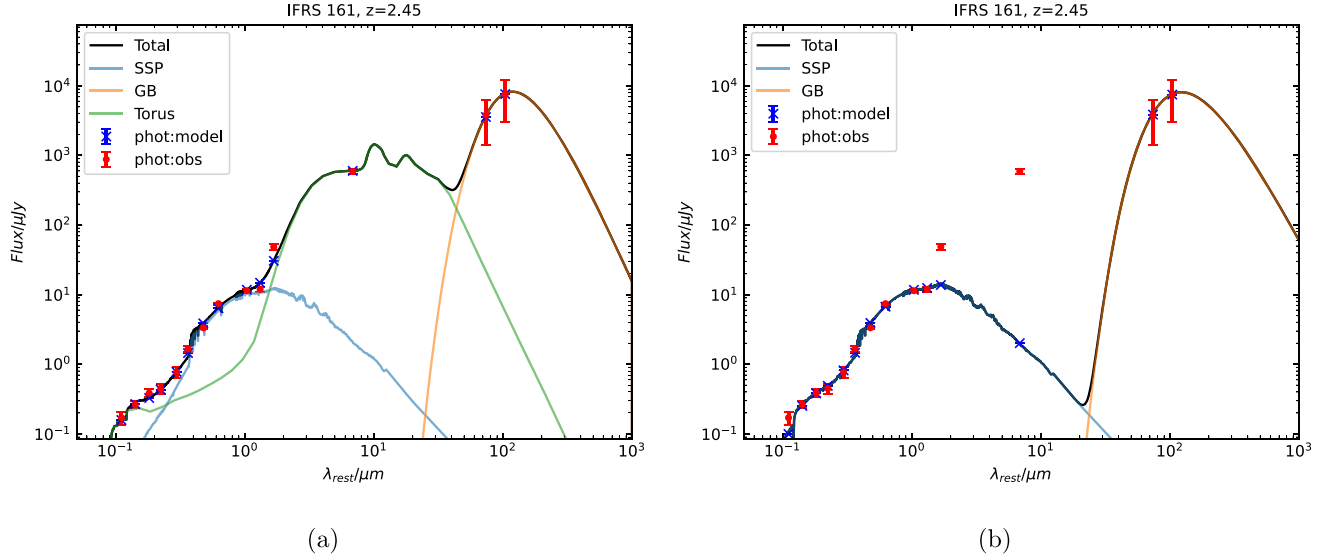
Figure 3. Left: the three-component (SSP+Torus+GB) model fit of IFRS 161. Right: the two-component (SSP+GB) model fit of IFRS 161. The red points with error bars represent the observed SED and the black solid lines represent the total model fit. The blue, green, and orange dashed lines represent the emissions from stars, AGNs, and dust, respectively.

Table 3
Summary of the Free Parameters and Priors

Parameters	SSP				GB		CLUMPY					
	$\log(\mathrm{age/yr})$	$\log(\tau/\mathrm{yr})$	$\log(Z/Z_\odot)$	A_v (mag)	T_{dust} (K)	β	N_0	Y	i	q	σ	τ_ν
Prior range	[5, 10.3]	[6, 12]	[−2.3, 0.7]	[0, 4]	[10, 100]	[1, 3]	[1, 15]	[5, 100]	[0, 90]	[0, 3]	[15, 70]	[10, 300]

Table 4
Bayesian Evidence of the SSP+Torus+GB Model and SSP+GB Model

Source ID	$\ln(\mathrm{ev_{AGN}})$	$\ln(\mathrm{ev_{no\ AGN}})$	$\ln\left(\frac{\mathrm{ev_{AGN}}}{\mathrm{ev_{no\ AGN}}}\right)$
122	−76.841 ± 0.46	−950.661 ± 0.422	873.77 ± 0.882
136	−88.215 ± 0.476	−209.998 ± 0.351	121.783 ± 0.827
154	−68.342 ± 0.534	−172.174 ± 0.339	103.832 ± 0.873
160	−108.569 ± 0.575	−6939.67 ± 0.526	6831.101 ± 1.101
161	−63.536 ± 0.386	−125.898 ± 0.326	62.362 ± 0.712
162	−184.425 ± 0.486	−742.109 ± 0.379	557.684 ± 0.865

green, and orange dashed lines, respectively. We adopted the median and 68% confidence intervals of the posterior probability distribution of each parameter as the fiducial value and uncertainties. The comparison of models and the derived properties will be discussed in the next section.

4.2. Median SED

In Figure 5, we present the best-fitting rest-frame SEDs of 20 IFRSs (gray lines) using the SSP+Torus+GB model. The SEDs are normalized to the luminosity at $\lambda = 1\,\mu\mathrm{m}$. Then we derived the median SED of the 20 normalized SEDs of IFRS, represented by the solid red line in Figure 5. We compare the median SED of the IFRS subsample with some known templates from M. Polletta et al. (2007), including a Type-1 QSO, a Type-2 QSO, starburst galaxy Arp 220, and AGN–starburst composite galaxy IRAS 19254−7245 South (hereafter I19254). We find that the median SED of IFRSs is similar to that of a Type-1 QSO at $0.1\,\mu\mathrm{m} < \lambda < 1\,\mu\mathrm{m}$. Within the range

∼1–1000 μm, the median SED is similar to that of I19254. Due to the lack of observational constraints on the FIR SED of most IFRSs, the rest-frame SEDs of the IFRS subsample exhibited a large dispersion in the FIR wavelength.

The normalized rest-frame SEDs of the IFRS sample exhibit two distinctive characteristics within the range $0.1\,\mu\mathrm{m} < \lambda < 1\,\mu\mathrm{m}$, showing a flat or a steep spectrum. We then divided the sample into two groups and derived the median SED for each group. One median SED shows great consistency with the Type-1 QSO SED throughout the UV-to-IR range, while the other is similar to the I19254 SED. Therefore, we believe that IFRSs could consist of at least two distinct populations. Possible reasons for this dichotomy will be discussed in Section 5.1.

5. Discussion

5.1. SED Dichotomy

Our study of the IFRS SEDs reveals two distinct groups within our sample (See Figure 6). One group exhibits SED characteristics similar to a Type-1 QSO, while the other group resembles AGN–starburst composites. Here, we explore the possible physical reasons behind these differences.

The evolutionary stage of the host galaxy and its central AGN can account for the observed SED variations. A Type-1 AGN might represent a more evolved state in which the AGN has cleared much of the surrounding dust and gas, revealing the central engine. In contrast, AGN–starburst composites could be in a transitional phase where intense starburst activity is still ongoing and the AGN is actively accreting material,
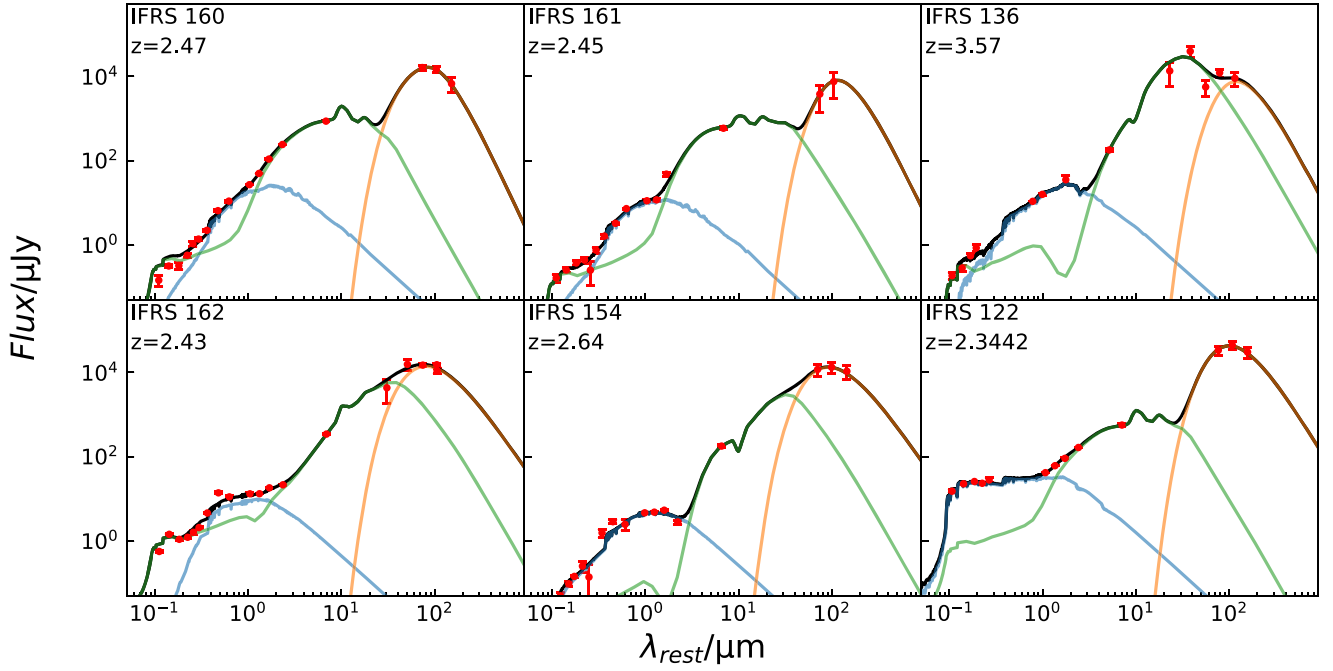
Figure 4. Best-fit three-component model SEDs for six IFRS in our sample. The source ID and redshift are shown in each panel. The red points with error bars represent the observed photometric data. The blue, green, and orange solid lines represent the emissions from stars, AGNs, and dust components, respectively. The solid black line represents the total SED.
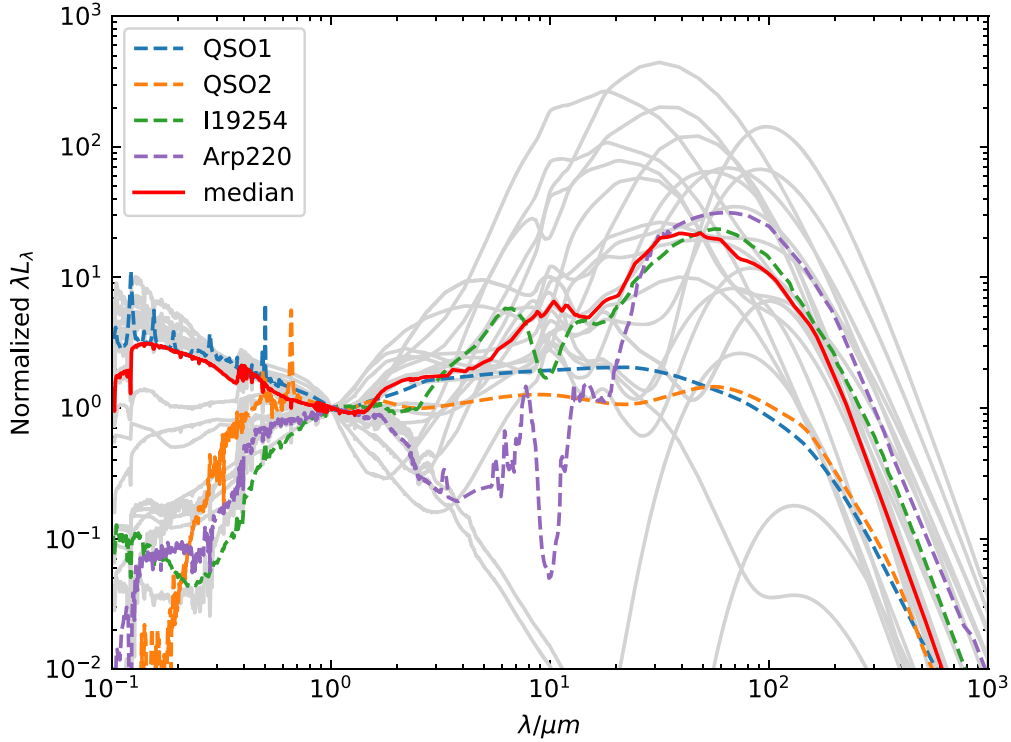

Figure 5. Normalized rest-frame SEDs (gray lines) and the median SED (red solid lines) of 25 IFRS. The SEDs are based on the best-fitting SSP+Torus+GB model and normalized to the luminosity at $\lambda = 1$ μm. Individual SEDs and the median SED are compared to templates from M. Polletta et al. (2007), including a Type-1 QSO, a Type-2 QSO, starburst galaxy Arp 220, and AGN–starburst composite galaxy IRAS 19254−7245 South (denoted as I19254). All SED templates are normalized to the luminosity at $\lambda = 1$ μm.

contributing to the composite SED. This scenario suggests that the relatively IR-bright IFRSs might be at an early stage along the AGN–starburst evolutionary sequence.

Differences in the distribution and amount of dust within the host galaxy can lead to distinct SED features. A Type-1 AGN typically shows less MIR and FIR emission due to the relatively lower amount of dust along our line of sight. In contrast, AGN–starburst composites have significant dust heated by both AGN and starburst activity, resulting in prominent MIR and FIR emission (C. J. Lonsdale et al. 2003). The IR-brighter sources in
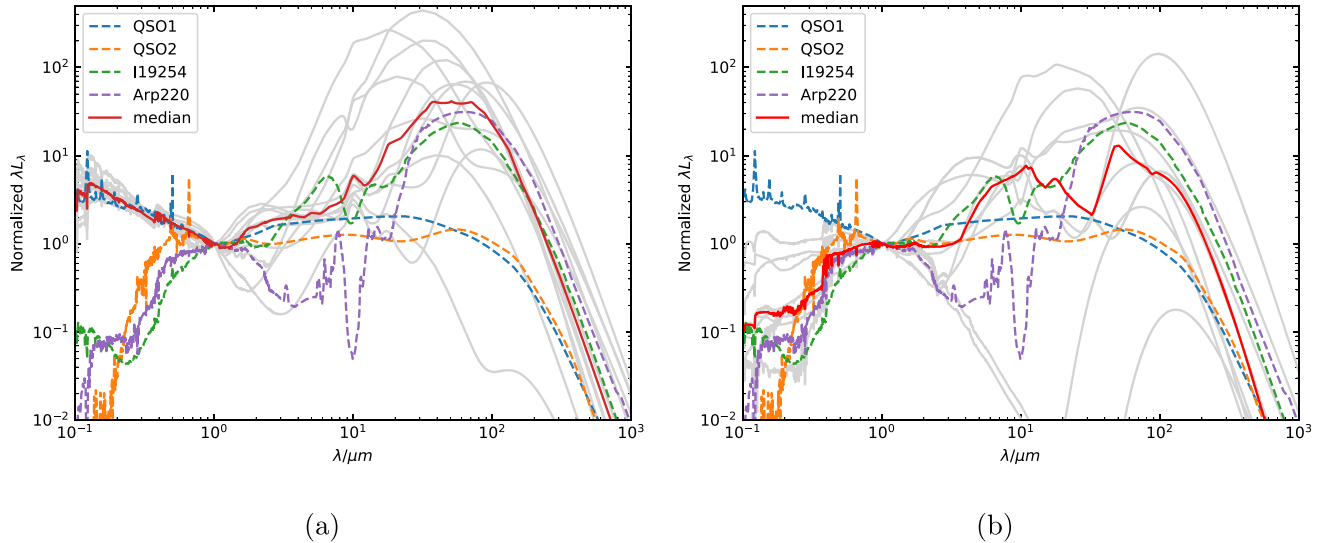
Figure 6. The median SEDs of two distinct groups. The median SED of IFRSs shows a flat spectrum (left) or a steep spectrum (right) at 0.1 μm $< \lambda <$ 10 μm.

our sample could result from additional dust obscuration. Variations in dust composition, grain size, and temperature can further modulate the observed SED. The dust properties derived from SED decomposition will be discussed in Section 5.4.

The intrinsic properties of the host galaxies, such as star formation rate (SFR), metallicity, and stellar population age, can also influence the SED. AGN–starburst composites are often found in galaxies with high SFRs, leading to strong FIR emission due to heated dust. In contrast, Type-1 AGN hosts may have lower SFRs, with the AGN dominating the SED (R. C. Hickox et al. 2014). Differences in the stellar population of the host galaxy and the properties of the interstellar medium can therefore contribute to the observed SED dichotomy. Our IFRS sample has a relatively low SFR according to the SED decomposition, which will be further discussed in Section 5.3.

While star-forming activities and dust obscuration in the host galaxy may contribute to the SED dichotomy observed in our IFRS sample, we cannot exclude the possibility that differences in the viewing angles of AGNs could also contribute to this dichotomy, as one subgroup also bears some resemblance to a Type-2 QSO. In a Type-2 QSO, the accretion disk and broad-line region are obscured by the torus, resulting in significant reduction or the complete absence of optical and UV emission in the observed SED (R. Antonucci 1993). However, it is important to note that the IFRS subgroup still shows higher IR luminosities than the Type-2 QSO template, indicating that there are multiple factors contributing to the SED dichotomy, such as the presence of dust. Therefore, the SED dichotomy in IFRSs is likely due to multiple factors, including the intrinsic properties of host galaxies and viewing angles.

5.2. IR–Radio Relation

The IR–radio relation is an important indicator of the emission mechanism in galaxies. In SFGs, the IR emission mainly originates from the reemission of dust particles, whereas the nonthermal radio emission primarily arises from synchrotron radiation in the supernova remnants. The IR and radio emissions in SFGs show a strong correlation because supernovae typically occur in young stellar populations.

Deviations from this correlation, caused by an excess of radio emission, usually imply the presence of an RL AGN.

We investigated the ratio of 24 μm MIR to 1.4 GHz radio flux densities of eight IFRSs with Spitzer/MIPS 24 μm observations, which is defined as $q_{24} = \log(S_{24\mu m}/S_{1.4GHz})$ (P. N. Appleton et al. 2004). The parameter q_{24} is conventionally used to distinguish between the populations of AGNs and SFGs. In Figure 7, we compare q_{24} of our IFRSs as a function of redshift with that of different types of populations, including starburst galaxies, AGN–starburst composites, and HzRGs from N. Seymour et al. (2007). The loci of Arp 220 and I19254 in the diagram q_{24}–z are determined using templates from M. Polletta et al. (2007). The eight IFRSs clearly deviate from the IR–radio flux density correlation of the SFGs and partially overlap with the population of HzRGs in Figure 7. The HzRGs from N. Seymour et al. (2007) have IR luminosity similar to that of luminous infrared galaxies and ultraluminous infrared galaxies (ULIRGs). Therefore, it seems likely that a fraction of the IFRSs in this paper represent the extension of the HzRGs at lower luminosities.

As illustrated in Figure 7, some IFRS have q_{24} between SFGs and HzRGs. Considering the similarity between the SEDs of IFRSs and the AGN–starburst composite I19254, it seems likely that some IFRSs consist of starburst galaxies with more prominent AGNs than I19254.

5.3. Star Formation Rate

We disentangled the IR emissions from AGN-heated warm dust and star formation-heated cold dust in SED modeling. In Table 5, we list the total IR luminosities (L_{IR}^{tot}), the IR luminosity of AGNs (L_{IR}^{AGN}), and that of the formation of stars (L_{IR}^{SF}) within the 8–1000 μm range. We found that the six FIR-detected IFRSs in our sample have fairly high IR luminosities ($L_{IR}^{tot} > 10^{12} L_\odot$), all of which exceed the limit of ULIRGs.

In Figure 8, we plot L_{IR}^{SF} versus L_{bol}^{AGN} and compare the six FIR detected IFRSs in our sample with different populations, including hot dust-obscured galaxies (Hot DOGs) at $z > 2$ (L. Fan et al. 2016; W. Sun et al. 2024), QSOs at $z \sim 2$ (Z. Ma & H. Yan 2015), and HzRGs at $1 < z < 4$ (G. Drouart et al. 2014). Previous research suggested that IFRSs could be a
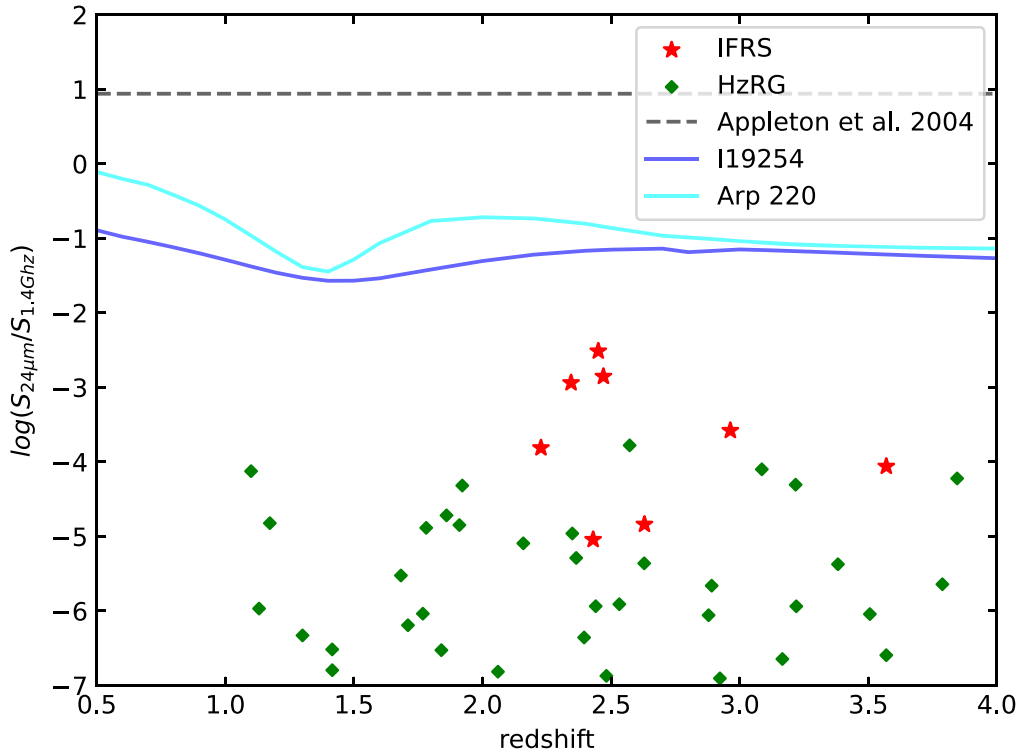
Figure 7. The flux density ratio between 24 μm and 1.4 GHz as a function of redshift. The red stars represent our IFRS sample and the green diamonds represent HzRGs from N. Seymour et al. (2007). The blue solid line and cyan solid line indicate the expected loci of I19254 and Arp 220 (M. Polletta et al. 2007). The black dashed line represents the typical value of $q_{24} \simeq 1.0$ for SFGs from P. N. Appleton et al. (2004).

Table 5
Summary of the Derived Properties of SED Modeling

Source ID	$\log(L_{IR}^{tot}/L_\odot)$	$\log(L_{IR}^{SF}/L_\odot)$	$\log(L_{IR}^{AGN}/L_\odot)$	T_{dust} (K)
122	$12.77^{+0.02}_{-0.03}$	$12.71^{+0.02}_{-0.02}$	$11.89^{+0.06}_{-0.07}$	$39.5^{+1.55}_{-1.52}$
136	$13.39^{+0.03}_{-0.01}$	$12.13^{+0.07}_{-0.04}$	$13.37^{+0.02}_{-0.01}$	$26.06^{+5.53}_{-5.18}$
154	$12.6^{+0.05}_{-0.03}$	$12.32^{+0.02}_{-0.01}$	$12.28^{+0.07}_{-0.07}$	$43.44^{+0.87}_{-0.73}$
160	$12.56^{+0.02}_{-0.01}$	$12.39^{+0.02}_{-0.02}$	$12.07^{+0.01}_{-0.01}$	$50.59^{+1.51}_{-2.13}$
161	$12.33^{+0.09}_{-0.07}$	$11.89^{+0.04}_{-0.02}$	$12.13^{+0.12}_{-0.1}$	$29.57^{+2.12}_{-1.48}$
162	$12.86^{+0.02}_{-0.02}$	$12.18^{+0.04}_{-0.02}$	$12.76^{+0.01}_{-0.02}$	$33.18^{+2.25}_{-2.07}$

weaker subgroup of HzRGs (J. D. Collier et al. 2014; A. Herzog et al. 2015b). Most of our IFRS sample lies at the low-luminosity end of HzRGs as illustrated in Figure 8.

Given the high IR luminosities of the FIR-detected IFRSs, we will use the simple relation between the SFR and IR luminosity for local galaxies (R. C. Kennicutt 1998):

$$\text{SFR} = 1.72 \times 10^{-10} \times L_{IR}^{SF} \qquad (5)$$

where L_{IR}^{SF} is in units of $L_\odot$ and SFR in $M_\odot \, \text{yr}^{-1}$. Our FIR-detected sample spans a small range of SFR, from 100 to 900 $M_\odot \, \text{yr}^{-1}$. Considering the nondetection in the FIR regime for a significant fraction of IFRSs, the SFR estimation of our sample could be an upper limit for the IFRS population. HzRGs span a much larger SFR range, from 100 to ~5000 $M_\odot \, \text{yr}^{-1}$ (G. Drouart et al. 2014), similar to that of submillimeter galaxies (SMGs) over the same redshift range (J. L. Wardlow et al. 2011; A. M. Swinbank et al. 2014).

The high radio luminosity and extreme radio-to-IR flux density ratio indicate strong AGN activities in IFRSs. However, despite the evidence for a significant impact of AGNs on host galaxies, the SFR of IFRSs in our sample showed no correlation with the AGN luminosity. It should be noted that the lack of correlation does not rule out a possible relationship between the two parameters because global star formation and AGN activity occur over different timescales, suggesting that estimations of the instantaneous AGN luminosity may not be closely related to its long-term average. Such variations may mask any underlying relationship (R. C. Hickox et al. 2014). Another reason for the observed lack of correlation could be the limited size of our IFRS sample, which can lead to stochastic variations that mask the potential correlation. In the future, we expect a larger IFRS sample with IR detection to testify to this correlation. Furthermore, as the SED dichotomy in Section 5.1 points out, IFRSs may represent a heterogeneous population at different evolutionary stages. Some IFRSs might be experiencing a surge in AGN activity with declining star formation. This diversity can obscure a clear correlation between AGN luminosity and SFR.

5.4. Dust Properties

In Table 5, we list the temperature of the cold dust in the IFRS subsample. The dust temperature of the IFRS ranges from 26 to 50 K, with a median value of 36.34 K. The derived dust temperatures are higher than those found in ULIRGs, SMGs, and DOGs on average, which range from 20 to 50 K (G. E. Magdis et al. 2010; J. Melbourne et al. 2012). In Figure 9, we plot the relation between the temperature of the cold dust T_{dust} and the IR luminosity of
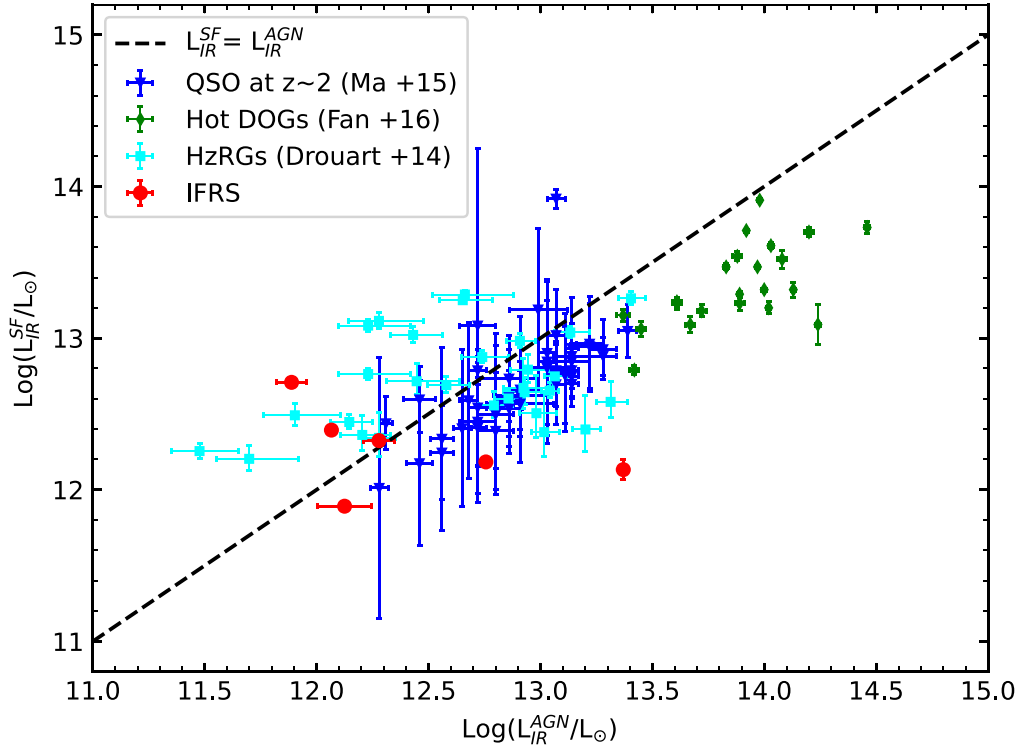
Figure 8. IR luminosity due to star-forming activities $L_{\mathrm{IR}}^{\mathrm{SF}}$ as a function of AGN IR luminosity for our IFRS sample and other populations: Hot DOGs at $z > 2$ (L. Fan et al. 2016; W. Sun et al. 2024), QSOs at $z \sim 2$ (Z. Ma & H. Yan 2015), and HzRGs at $1 < z < 4$ (G. Drouart et al. 2014).
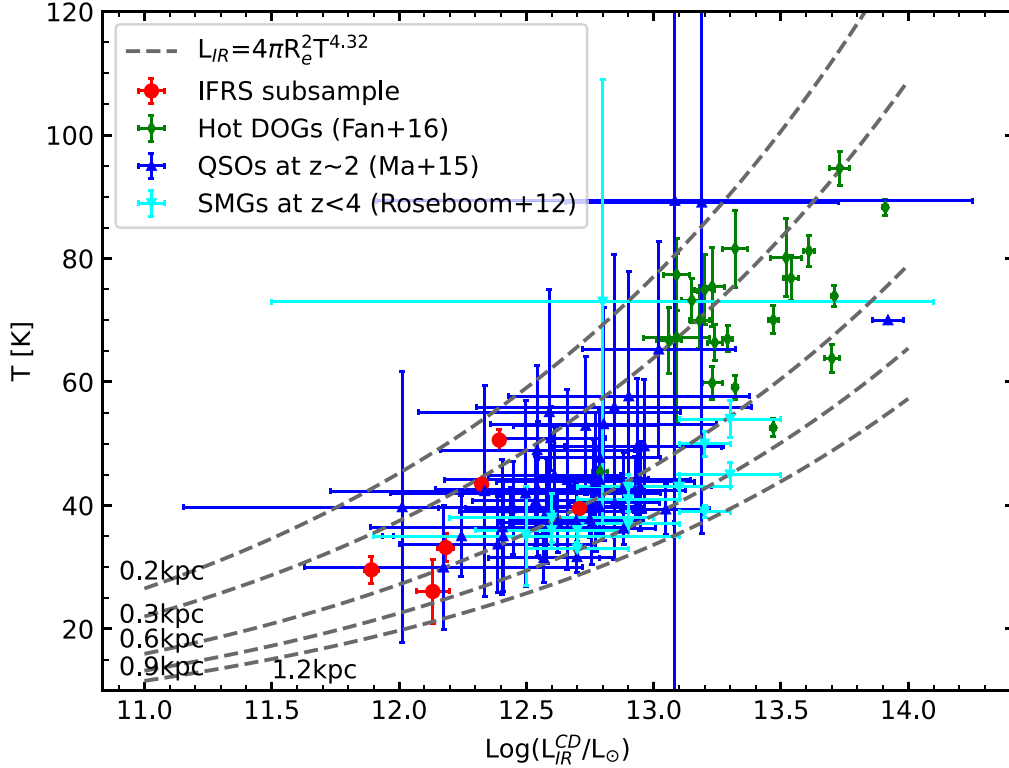
Figure 9. Cold dust temperature as a function of IR luminosity for our IFRS sample and other populations: Hot DOGs at $z > 2$ (L. Fan et al. 2016; W. Sun et al. 2024), QSOs at $z \sim 2$ (Z. Ma & H. Yan 2015), and SMGs at $z < 4$ (I. G. Roseboom et al. 2012). The gray dashed lines represent the T_{dust}–L_{IR} relation with different R_e values (0.2, 0.3, 0.6, 0.9, and 1.2 kpc).

the cold dust. We compare our IFRS sample with other populations: Hot DOGs at $z > 2$ (L. Fan et al. 2016; W. Sun et al. 2024), QSOs at $z \sim 2$ (Z. Ma & H. Yan 2015), and SMGs at $z < 4$ (I. G. Roseboom et al. 2012). The compared samples also used the graybody model described by Equation (4).

The locus of our IFRS sample in the T_{dust}–L_{IR} plane is consistent with that of the QSO sample at $z \sim 2$, but the QSO sample from Z. Ma & H. Yan (2015) is slightly more luminous and has a higher dust temperature. Recall that for a perfect blackbody, the Stefan–Boltzmann law gives $L = 4\pi R^2 \sigma T^4$. According to Z. Ma & H. Yan (2015), the equivalent for a graybody with general opacity should follow $L_{IR} = 4\pi R_e^2 \sigma T^\alpha$, where R_e could be interpreted as the effective radius of the FIR-emitting region of a galaxy. The value of the index α depends on the choice of the dust temperature range. We adopt the value 4.32 for index α given by Z. Ma & H. Yan (2015) in Figure 9. We plot the T_{dust}–L_{IR} relation following the modified graybody equation with a series of different R_e (0.2, 0.3, 0.6, 0.9, and 1.2 kpc; see the gray dashed lines in Figure 9). Our IFRS subsample spans a relatively small range in R_e (from 0.3 to 0.6 kpc), indicating that the increase in the IR luminosity of cold dust is mainly due to the increase in its temperature.

It is important to note that the sample selection of our analysis targets the brighter IFRSs. As a result, the derived properties and statistical distributions might be biased, limiting the applicability of these results to the fainter members of the IFRS population. The diversity in the spectral indices among the IFRSs also suggests that they should not be treated as a homogeneous source population. The fainter IFRSs that are undetectable at IR wavelengths may exhibit different physical properties to those included in our sample. Future studies incorporating a more comprehensive sample and a deeper IR survey are needed to verify the robustness of the conclusions drawn here.

6. Summary

In this paper, we present an optical to IR SED analysis of 20 IFRSs with spectroscopic redshift at $1 < z < 4$. We construct the SED by combining SDSS, Spitzer IRAC and MIPS, Herschel PACS and SPIRE data, and other available optical and IR observations. We used an updated version of BayeSED to model the observed SED and infer the physical properties of our IFRS sample, such as the IR luminosity and dust temperature. Our main results are summarized as follows:

1. We compare Bayesian evidence for the three-component model (SSP+Torus+GB) and the two-component model (SSP+GB). We find that the three-component model has more Bayesian evidence than the two-component model for all FIR-detected IFRSs in our sample, indicating that the IFRSs are most likely to be AGNs.
2. We construct a median IFRS SED by taking the median value of 20 normalized rest-frame SEDs of 20 IFRSs. We categorize our sample into two groups based on their luminosity ratios between optical and mid-IR. The median SEDs of the two groups show similarities with SED templates of a Type-1 QSO and an AGN–starburst composite, respectively, suggesting that IFRSs are made up of at least two different populations.
3. The FIR-detected IFRSs in our sample have a relatively high IR luminosity, with a typical value of $\log(L_{IR}/L_\odot) \sim 12.69^{+0.04}_{-0.03}$. We disentangle the IR luminosity of AGNs and star formation and find the contributions from the two components to be approximately equal. We estimate the upper limit of the SFR of IFRSs to be $\sim$900 $M_\odot$ yr^{-1}. The SFRs of our IFRS sample show no correlation to the AGN luminosity,

despite a clear indication of AGN impact on host galaxies. The observed dichotomy in SED characteristics is likely due to different evolutionary stages, with some sources being dominated by AGN activity, while others exhibit significant starburst activity alongside AGN features.

4. Our IFRS subsample has relatively low dust temperatures, with a typical value of $T_{dust} \sim 36.34^{+1.90}_{-1.79}$ K. Adopting the T_{dust}–L_{IR} relation of $L_{IR} = 4\pi R_e^2 \sigma T^{4.32}$, we find that the IFRS subsample spans a relatively small range in R_e, suggesting that the increase in the IR luminosity of the cold dust is mainly due to the increase in its temperature.

Future deeper IR surveys will be crucial in providing more comprehensive data on IFRSs, enabling more robust conclusions about their physical properties and evolutionary pathways. These surveys will help us better understand the connection between AGN activity and star formation, shedding light on the role of IFRSs in galaxy evolution at high redshifts. Enhanced infrared sensitivity and coverage will allow us to detect fainter counterparts and improve the representativeness of our samples, ultimately advancing our knowledge of these enigmatic sources.

ORCID iDs

Yihang Zhang (张迤航) ● https://orcid.org/0009-0003-9423-2397
Lulu Fan (范璐璐) ● https://orcid.org/0000-0003-4200-4432
Tao An (安涛) ● https://orcid.org/0000-0003-4341-0029
Jun Yang (杨军) ● https://orcid.org/0000-0002-2322-5232
Weibin Sun (孙卫斌) ● https://orcid.org/0009-0004-7885-5882
Haoran Yu (于浩然) ● https://orcid.org/0009-0008-1319-498X
Yunkun Han (韩云坤) ● https://orcid.org/0000-0002-2547-0434

References

Abdurro'uf, Accetta, K., Aerts, C., et al. 2022, ApJS, 259, 35
Ahn, C. P., Alexandroff, R., Allende Prieto, C., et al. 2012, ApJS, 203, 21
Antonucci, R. 1993, ARA&A, 31, 473
Appleton, P. N., Fadda, D. T., Marleau, F. R., et al. 2004, ApJS, 154, 147
Becker, R. H., White, R. L., & Helfand, D. J. 1995, ApJ, 450, 559

Bruzual, G., & Charlot, S. 2003, MNRAS, 344, 1000

Calzetti, D., Armus, L., Bohlin, R. C., et al. 2000, ApJ, 533, 682

Cardamone, C. N., van Dokkum, P. G., Urry, C. M., et al. 2010, ApJS, 189, 270

Chabrier, G. 2003, PASP, 115, 763

Collier, J. D., Banfield, J. K., Norris, R. P., et al. 2014, MNRAS, 439, 545

Condon, J. J., Cotton, W. D., Greisen, E. W., et al. 1998, AJ, 115, 1693

Cutri, R. M., Wright, E. L., Conrow, T., et al. 2021, yCat, 2328, 0

De Breuck, C., Seymour, N., Stern, D., et al. 2010, ApJ, 725, 36

DESI Collaboration, Adame, A. G., Aguilar, J., et al. 2024, AJ, 168, 58

Drouart, G., De Breuck, C., Vernet, J., et al. 2014, A&A, 566, A53

Fan, L., Han, Y., Nikutta, R., Drouart, G., & Knudsen, K. K. 2016, ApJ, 823, 107

Fazio, G. G., Hora, J. L., Allen, L. E., et al. 2004, ApJS, 154, 10

Garn, T., & Alexander, P. 2008, MNRAS, 391, 1000

Gregory, P. C., Scott, W. K., Douglas, K., & Condon, J. J. 1996, ApJS, 103, 427

Griffin, M. J., Abergel, A., Abreu, A., et al. 2010, A&A, 518, L3

Han, Y., Fan, L., Zheng, X. Z., Bai, J.-M., & Han, Z. 2023, ApJS, 269, 39

Han, Y., & Han, Z. 2014, ApJS, 215, 2

Han, Y., & Han, Z. 2019, ApJS, 240, 3

Herzog, A., Middelberg, E., Norris, R. P., et al. 2014, A&A, 567, A104

Herzog, A., Middelberg, E., Norris, R. P., et al. 2015a, A&A, 578, A67

Herzog, A., Norris, R. P., Middelberg, E., et al. 2015b, A&A, 580, A7

Herzog, A., Norris, R. P., Middelberg, E., et al. 2016, A&A, 593, A130

Hickox, R. C., Mullaney, J. R., Alexander, D. M., et al. 2014, ApJ, 782, 9

Hudelot, P., Cuillandre, J. C., Withington, K., et al. 2012, yCat, 2317, 0

Huynh, M. T., Norris, R. P., Siana, B., & Middelberg, E. 2010, ApJ, 710, 698

Jarvis, M. J., Bonfield, D. G., Bruce, V. A., et al. 2013, MNRAS, 428, 2

Kennicutt, R. C., Jr. 1998, ARA&A, 36, 189

Kimball, A. E., & Ivezić, Ž. 2008, AJ, 136, 684

Kimball, A. E., & Ivezić, Ž. 2014, in IAU Symp. 304, Multiwavelength AGN Surveys and Studies, ed. A. M. Mickaelian & D. B. Sanders (Cambridge: Cambridge Univ. Press), 238

Lawrence, A., Warren, S. J., Almaini, O., et al. 2012, yCat 2314, 0

Lonsdale, C. J., Lonsdale, C. J., Smith, H. E., & Diamond, P. J. 2003, ApJ, 592, 804

Ma, Z., & Yan, H. 2015, ApJ, 811, 58

Magdis, G. E., Elbaz, D., Hwang, H. S., et al. 2010, MNRAS, 409, 22

Melbourne, J., Soifer, B. T., Desai, V., et al. 2012, AJ, 143, 125

Middelberg, E., Norris, R. P., Cornwell, T. J., et al. 2008a, AJ, 135, 1276

Middelberg, E., Norris, R. P., Hales, C. A., et al. 2011, A&A, 526, A8

Middelberg, E., Norris, R. P., Tingay, S., et al. 2008b, A&A, 491, 435

Nenkova, M., Sirocky, M. M., Ivezić, Ž., & Elitzur, M. 2008a, ApJ, 685, 147

Nenkova, M., Sirocky, M. M., Nikutta, R., Ivezić, Ž., & Elitzur, M. 2008b, ApJ, 685, 160

Norris, R. P., Afonso, J., Appleton, P. N., et al. 2006, AJ, 132, 2409

Norris, R. P., Afonso, J., Cava, A., et al. 2011, ApJ, 736, 55

Norris, R. P., Tingay, S., Phillips, C., et al. 2007, MNRAS, 378, 1434

Oliver, S. J., Bock, J., Altieri, B., et al. 2012, MNRAS, 424, 1614

Orenstein, B. J., Collier, J. D., & Norris, R. P. 2019, MNRAS, 484, 1021

Poglitsch, A., Waelkens, C., Geis, N., et al. 2010, A&A, 518, L2

Polletta, M., Tajer, M., Maraschi, L., et al. 2007, ApJ, 663, 81

Randall, K. E., Hopkins, A. M., Norris, R. P., & Edwards, P. G. 2011, MNRAS, 416, 1135

Rengelink, R. B., Tang, Y., de Bruyn, A. G., et al. 1997, A&AS, 124, 259

Rieke, G. H., Young, E. T., Engelbracht, C. W., et al. 2004, ApJS, 154, 25

Robert, C. P., Chopin, N., & Rousseau, J. 2009, StaSc, 24, 2

Roseboom, I. G., Ivison, R. J., Greve, T. R., et al. 2012, MNRAS, 419, 2758

Seymour, N., Stern, D., De Breuck, C., et al. 2007, ApJS, 171, 353

Singh, V., Wadadekar, Y., Ishwara-Chandra, C. H., et al. 2017, MNRAS, 470, 4956

Spitzer Science Center (SSC), Infrared Science Archive (IRSA) 2021, yCat, 2368, 0

Sun, W., Fan, L., Han, Y., et al. 2024, ApJ, 964, 95

Swinbank, A. M., Simpson, J. M., Smail, I., et al. 2014, MNRAS, 438, 1267

Trotta, R. 2008, ConPh, 49, 71

Wardlow, J. L., Smail, I., Coppin, K. E. K., et al. 2011, MNRAS, 415, 1479

Wright, E. L., Eisenhardt, P. R. M., Mainzer, A. K., et al. 2010, AJ, 140, 1868

Zinn, P. C., Middelberg, E., & Ibar, E. 2011, A&A, 531, A14